

PAPER • OPEN ACCESS

Multifunctional shape-memory smart window based on femtosecond-laser-printed photothermal microwalls




To cite this article: Chao Chen *et al* 2025 *Int. J. Extrem. Manuf.* **7** 015504

View the [article online](#) for updates and enhancements.

You may also like

- [Fine structural and photoluminescence properties of Mg₂Si nanosheet bundles rooted on Si substrates](#)
Tomoya Koga, Ryo Tamaki, Xiang Meng et al.
- [Efficient concentration of trace analyte with ordered hotspot construction for a robust and sensitive SERS platform](#)
Youdi Hu, Yanlei Hu, Zhenyu Wang et al.
- [Magnetically-responsive microwall arrays with path-guide for directional transportation of droplets](#)
Soyeon Kwon, Jihun Kim, Yoobin Do et al.

Multifunctional shape-memory smart window based on femtosecond-laser-printed photothermal microwalls

Chao Chen^{1,*} , Sijia Guo¹, Long Zhang¹, Hao Yao¹, Bingrui Liu^{2,*}, Chenchu Zhang³ , Yachao Zhang⁴, Zhaoxin Lao⁴, Sizhu Wu^{4,*} and Dong Wu⁵ 

¹ Department of Materials Physics and New Energy Device, School of Materials Science and Engineering, Hefei University of Technology, Hefei 230009, People's Republic of China

² Department of Environmental Science and Engineering, School of Resources and Environment, Anhui Agricultural University, Hefei 230036, People's Republic of China

³ Institute of Industry and Equipment Technology, Hefei University of Technology, Hefei 230009, People's Republic of China

⁴ School of Instrument Science and Opto-Electronics Engineering, Hefei University of Technology, Hefei 230009, People's Republic of China

⁵ Department of Precision Machinery and Precision Instrumentation, University of Science and Technology of China, Hefei 230026, People's Republic of China

E-mail: chaoc11@ustc.edu.cn, brliu@ustc.edu.cn and sizhuwu@hfut.edu.cn

Received 12 April 2024, revised 4 June 2024

Accepted for publication 14 October 2024

Published 5 November 2024



CrossMark

Abstract

Smart windows (SWs) garner significant potential in green buildings owing to their capability of on-demand tuning the solar gains. Apart from solar regulation, people always desire a type of slippery SW which can repel the surface hydrous contaminants for anti-fouling application. Unfortunately, the up-to-date slippery SWs that respond to electrical/thermal stimuli have drawbacks of inferior durability and high energy-consumption, which greatly constrain their practical usability. This article presents our current work on an ultra-robust and energy-efficient near-infrared-responsive smart window (NIR-SW) which can regulate the optical transmittance and droplet's adhesion in synergy. Significantly, laser-printing strategy enables us to seed the shape-memory photothermal microwalls on a transparent substrate, which can promote daylighting while maintaining privacy by near-infrared (NIR) switching between being transparent and opaque. As a light manipulator, it turns transparent with NIR-activated erect microwalls like an open louver; however, it turns opaque with the pressure-fixed bent microwalls akin to a closed louver. Simultaneously, the droplets can easily slip on the surface of erect microwalls similar to a classical lotus effect; by contrast, the droplets will tightly pin on the surface of bent microwalls analogous to the prevalent rose effect. Owing to shape-memory effect, this optical/wettability regulation is thus reversible and reconfigurable in response to the

* Authors to whom any correspondence should be addressed.



Original content from this work may be used under the terms of the [Creative Commons Attribution 4.0 licence](https://creativecommons.org/licenses/by/4.0/). Any further distribution of this work must maintain attribution to the author(s) and the title of the work, journal citation and DOI.

alternate NIR/pressure trigger. Moreover, NIR-SW unfolds a superior longevity despite suffering from the raindrop's impacting more than 10 000 cycles. Remarkably, such a new-type SW is competent for thermal management, anti-icing system, peep-proof screen, and programmable optics. This work renders impetus for the researchers striving for self-cleaning intelligent windows, energy-efficient greenhouse, and so forth.

Supplementary material for this article is available [online](#)

Keywords: femtosecond laser, slippery surface, photothermal microwalls, controllable wettability, switchable transparency

1. Introduction

As the rapid development of society and industry, energy consumption in buildings accounts for about 40% of total energy consumption, which has aroused the increasing attention for human beings [1–3]. Fortunately, as the promising envelope of buildings, smart windows (SWs) with tunable clarity could greatly alleviate above-mentioned issue through regulating the transmittance and reflectance of solar radiation, thereby improving the indoor comfort independent of air-conditioning facility [4–6]. Accordingly, a diversity of SWs that respond to heat [7–9], electric field [10, 11], pH [12], chemical salt [13], humidity [14] and mechanical stress [15, 16] have been developed to fine-tune the luminous flux of sunlight. Apart from above conventional SWs, a novel type of SW based on dielectric elastomer actuators also springs up in very recent years. Leveraging a strain-induced micro-wrinkling and the reverse by electric-field-induced unfolding, their surface optical visibility could be on-demand switched between transparent state and translucent state [17–20]. Otherwise, Li *et al* reported a mechanoresponsive SW by vertically fixing the $\text{Fe}_3\text{O}_4@/\text{SiO}_2$ nanochains array in an elastic polyacrylamide matrix, which enabled the optical transmittance to vary from the transparent state of 65% to the opaque state of 10% under a shear-strain stimulus [21]. Through grafting a droplet-based electricity generator, Wang and co-workers put forward a self-powered cholesteric liquid crystal SW, which could experience a reversible conversion between high clarity and low clarity with the water-impact-induced electrical power [22]. More recently, Chen *et al* proposed a thermo-chromic SW made of thermo-activated P(NIPAM-*co*-DMAA) hydrogel, which acted as a highly efficient light-modulator for all-weather comfort regulation [23]. Despite extensive progress in SWs, unfortunately, the inevitable contaminants (*e.g.* muddy water, organics, and such) would severely deteriorate their optically switching performance, especially in dim rainy days [24–26]. As a result, the self-cleaning SWs with dually-switchable wettability and transparency are needed.

Inspired by natural *Nepenthes* plant, Aizenberg and coworkers pioneeringly developed a state-of-the-art slippery SW which was accountable for the dynamic adjustment of optical transparency and wettability via a graded mechanical stimulus [27]. The manipulating principle is that when

the monoaxial stretch was applied, the fallen lubricant within the nano-porous elastic film would alter its original smooth and defect-free surface towards a rough topography, thereby achieving the reversible conversion between a transparent/slipping state and an opaque/pinning state. Following this classical method, Yao *et al* prepared a type of thermo-actuated slippery SW based on organogel which was made of paraffin wax and polydimethylsiloxane (PDMS) [28]. Through manoeuvring the phase change of *n*-paraffin, its interfacial architecture was thermally activated to transform between air/liquid/solid system and air/solid/solid system, thereby regulating the optical transmitting and the drop's wetting properties in synergy. On this basis, a diversity of liquid-mediated slippery SWs were in success explored for manipulating the optical and wetting performance [29–31]. Upon the deposition and evaporation of refractive-index-matched liquids (*e.g.* acetic acid, glycol, ethanol) within the porous substrates (*e.g.* SiO_2 , PTFE), the appearance of these devices could be dynamically glazing and the surface drops simultaneously unfolded a switchable wetting behaviour, which was supposed to be determined by their local roughness [32, 33]. Though ceaseless endeavours had been dedicated to bloom the slippery SWs, several blockages arise subsequently. (i) These slippery liquid-infused SWs suffering from severe viscous dissipation would decrease their longevity [27–33]. (ii) Despite a durable electric-triggered SW had been explored, which has a considerable disadvantage of energy consumption [34]. In consequence, developing an ultra-robust and energy-saving slippery SW is highly desirable yet challenging to date.

To answer above challenges, we propose an ultra-durable NIR-SW by seeding the laser-printed carbon-black-doped shape-memory microwalls on a transparent platform. Once the pressure (~ 5 N) was applied, the microwalls turn to bend for shielding the incident light which enables an opaque visibility. However, owing to a shape-memory effect, these bent microwalls will recover to its original erect morphology for a transparent state under a remote NIR heating process. According to this principle, the shape-memory NIR-SW could be dynamically glazing with the function of 808 nm NIR trigger and stress stimulus. Simultaneously, the tunable topography over microwalls can switch their surface adhesion force for repelling or capturing diverse droplets which is beneficial for self-cleaning and antifouling SWs. (figure 1;

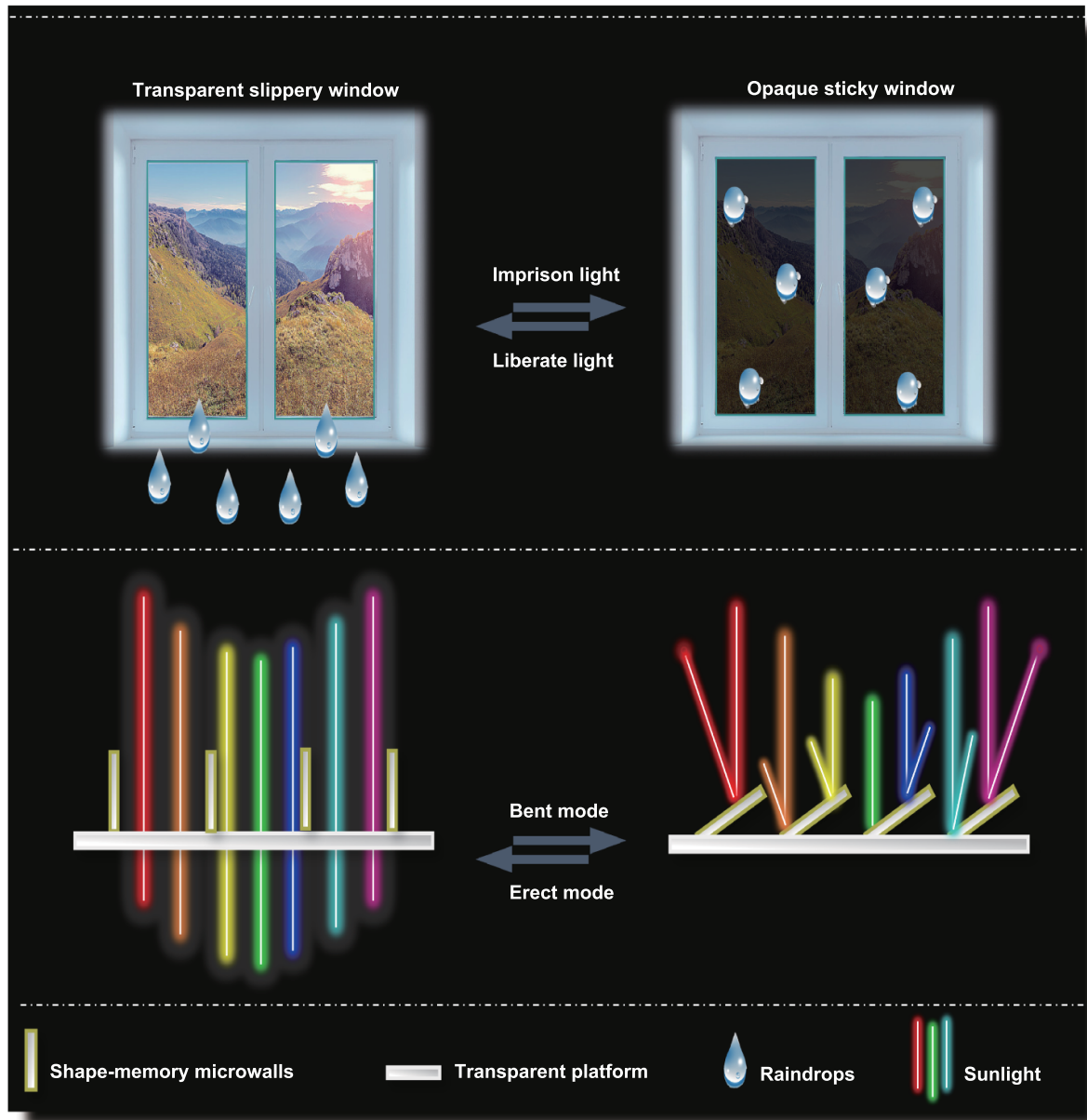


Figure 1. Conceptual hypothesis over a wettability-controllable SW. The targeted bi-functional SW should be dually-switchable between a transparent slippery state and an opaque sticky state in response to an alternate stress/light trigger (the upper diagram). As a result, the architecture of a desirable SW should integrate the CB-doped shape-memory microwalls together with an underlying transparent supporter (the lower diagram).

supporting information, movie S1). Thermal infrared imaging technique coupling with high-speed photography enables us to shed light on the steering thermodynamics and hydrokinetics. Significantly, all-solid-state NIR-SW can undergo the continuous raindrop's striking more than 10 000 cycles. Lastly, by integrating an optimized NIR-SW, multifunctional scenarios including thermal management, anti-icing system, peep-proof screen and optical encoder were displayed. This work provides inspirations for the researchers in the fields of micro/nano-fabrications, antifouling optics, self-cleaning intelligent windows, energy-efficient greenhouse, and so on.

2. Results and discussion

2.1. Facile manufacture of slippery shape-memory NIR-SW

A desirable NIR-SW should be integrated by two pivotal components: the highly-arrayed NIR-actuated photothermal microwalls with shape-memory property as the dimming cells and an underlying transparent supporting platform for the integration with above microwalls. In this regard, the preparing protocol of this dimming device should be divided into four procedures that were simplified as (i) laser grooving, (ii) infusion of the matrix of carbon black (CB) and shape-memory

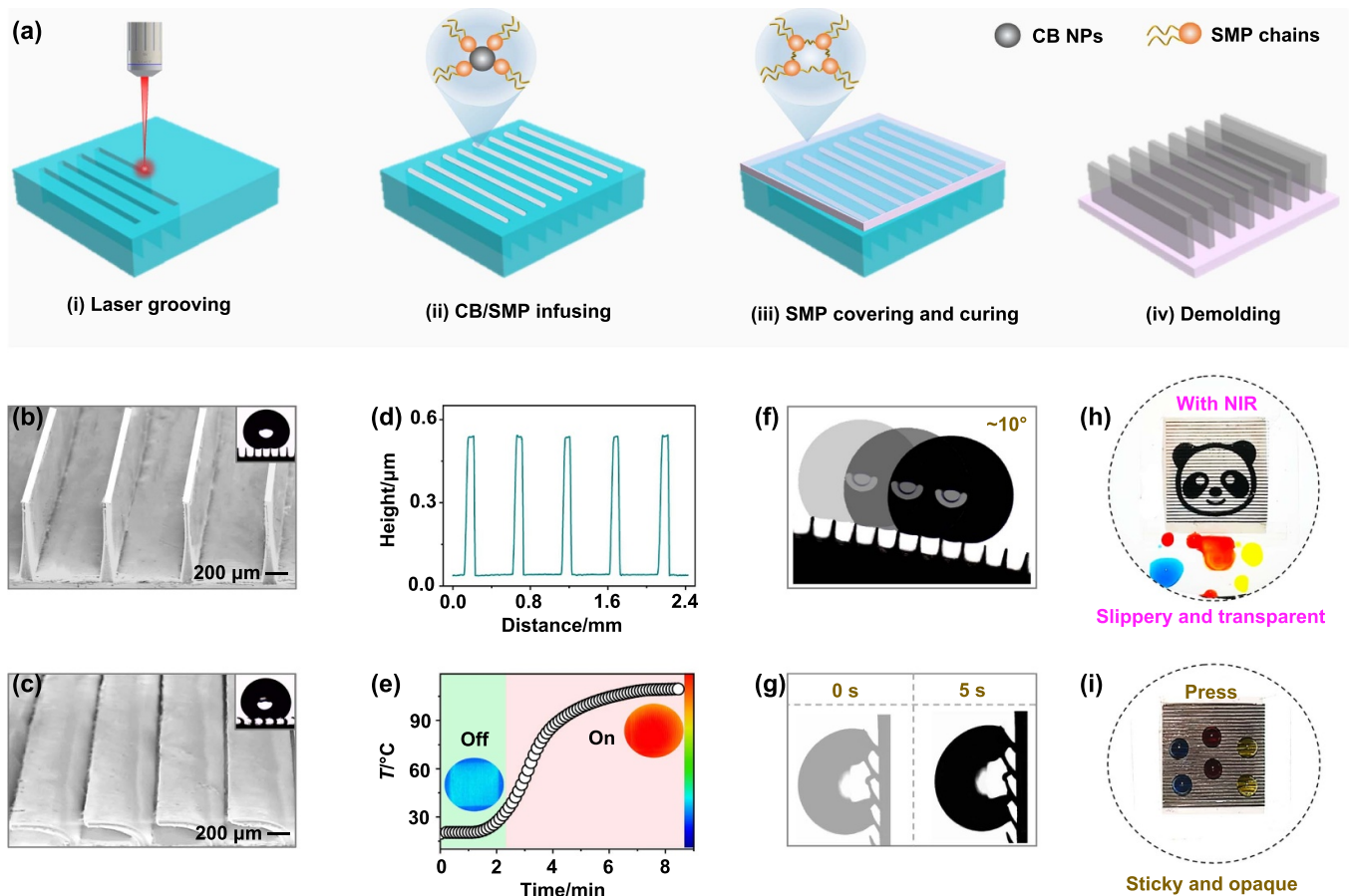


Figure 2. Facile fabrication of dual-functional NIR-SW by femtosecond laser. (a) Schematic diagram for harvesting the desirable NIR-SW including laser-grooving PTFE template, CB/SMP matrix infusing, pure SMP gel covering, and a subsequent demoulding process. Morphology imaging by SEM for the light-triggered shape-memory (b) erect microwalls and (c) bent microwalls. The scale bar is 0.5 mm; The insets display their apparent hydrophobicity. (d) 3D confocal microscopic profile for the as-prepared erect-mode NIR-SW. (e) Temperature-time curve for the NIR-SW irradiated by a near-infrared lamp; the insets refer to the thermal infrared images over light-triggered NIR-SW. (f)–(g) The critical sliding angles by CCD camera for characterizing the migrating dynamics of droplets ($\sim 10 \mu\text{l}$) on dual-mode tilt NIR-SW. Digital clips for the NIR-SW dually-switching between (h) opaque state with pronounced hysteresis and (i) transparent state with smaller hysteresis that responds to the alternative light/stress trigger. The results showcases that current NIR-SW serves not only a wettability manipulator but also a transparency actuator, which grants a remote, energy-efficient and all solid-state merit.

polymer (SMP), (iii) covering the pure SMP gel, and (iv) curing for a final demoulding operation, as shown in figure 2(a).

Accordingly, (i) we take advantage of femtosecond laser to rapidly machine an array of parallel grooves on a PTFE membrane with the thickness of 0.5 mm, which was subsequently utilized as a transfer template, as shown in figure 2(a-i). Wherein, femtosecond laser is almost adaptive for processing micro-structures on all existing materials (e.g. metals, glass, plastic, crystals) due to its unique advantages of giant peak power and low thermal effect, which is far superior to the traditional nanosecond laser or picosecond laser [35–41]. Thereafter, (ii) a uniform hybrid of CB/SMP with mass concentration $\sim 5 \text{ mg}\cdot\text{ml}^{-1}$ could be readily infused into above grooves under the help of vacuum-pumping apparatus for 30 min, where the residual hybrid should be removed by a doctor-blade method, as shown in figures 2(a-ii). (iii) We then cover the pure SMP gel onto above semi-product

via a spin-coating process (500 rpm, 1 min), which was subsequently annealed to cure at 65°C for 4 h, as shown in figure 2(a-iii). Finally, (iv) the NIR-SW could be successfully divorced from the PTFE template through manual lifting, as shown in figure 2(a-iv). Scanning electron microscope (SEM) and 3D profilometer collaboratively witness that the laser-printed microwalls display the highly-uniform height, half-width and interval that were approximately quantified as 0.5 mm, 0.1 mm and 0.5 mm, as shown in figures 2(b) and (d) and figure S1. The inset verified that the resultant NIR-SW has a superhydrophobic appearance with a water contact angle (WCA) of $\sim 156^\circ$. Once the near infrared light irradiates on the erect shape-memory microwalls, the photo-thermal effect would elevate the surface temperature above its glass-transition temperature (T_g) leading to an elastic state, as shown in figure 2(e). Therein, the erect shape-memory microwalls could be pressed to a bent mode after cooling

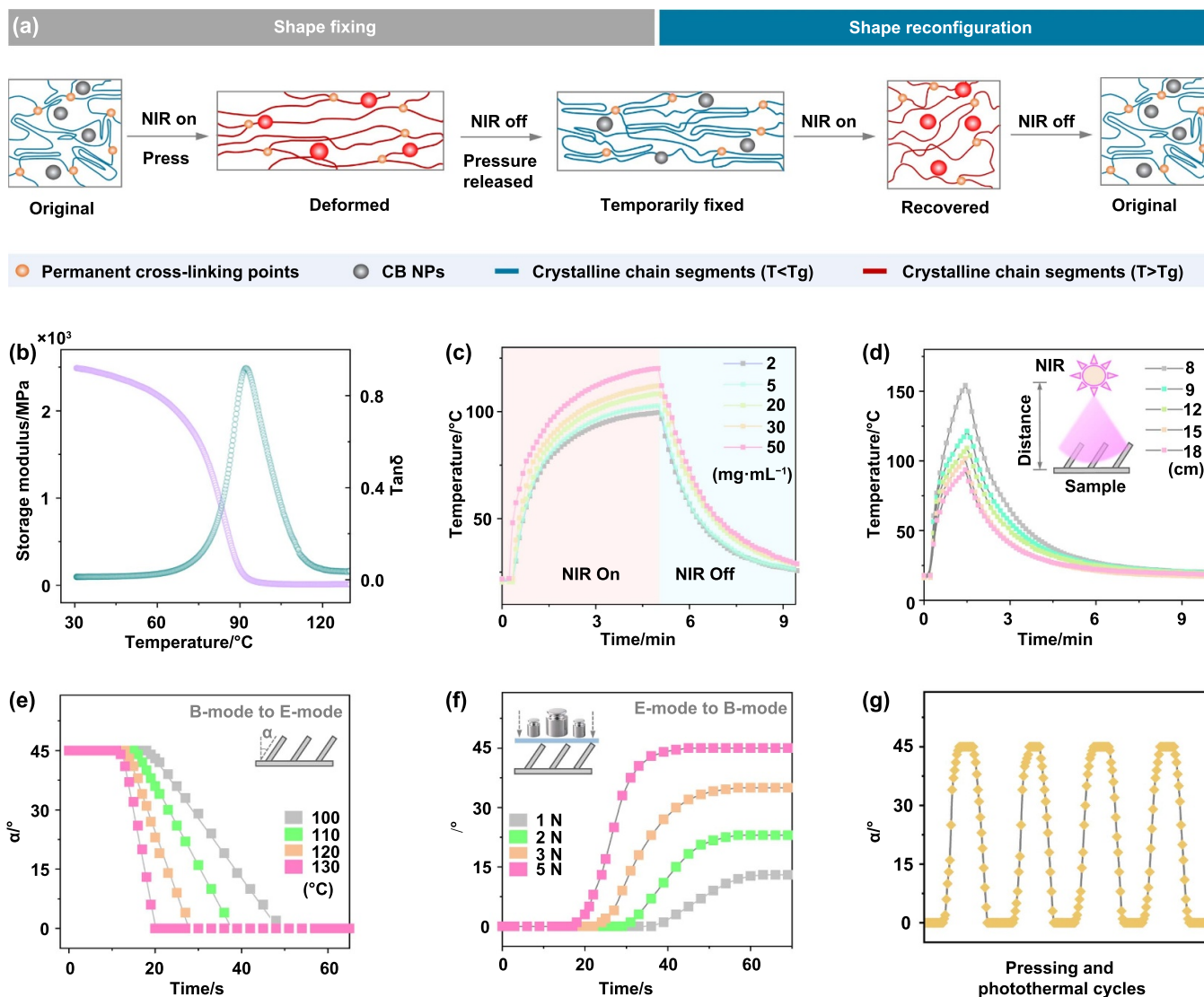


Figure 3. Underlying thermodynamics over shape-memory NIR-SW. (a) Schematic diagram for uncovering the reconfigurable mechanism of CB/SMP microwalls between the temporary bent state and the permanent erect state on the basis of the shape-memory effect coupling with the photothermal effect. (b) Dynamic mechanical analysis (DMA) for clarifying the glass-transition temperature T_g of CB/SMP microwalls. The surface temperature variation as the light-loading duration over NIR-SW with different (c) CB concentration and (d) light-irradiating distance. The evolution of microwall's bent angle α as a function of (e) surface temperature and (f) applied pressure. The results indicate the larger surface temperature and loading pressure would contribute to elevate the shape-morphing sensitivity. (g) Mechanical reliability test over NIR suffering from cyclic pressing/photothermal operations. The result manifest current shape-memory NIR-SW has a good thermodynamic stability.

the surface temperature below T_g for its glassy state, as shown in figure 2(c). By this token, the NIR-SW could be reversibly switched between a slippery state with the water sliding angle (WSA) $\sim 10^{\circ}$ and a sticky state (pinning at 90°), as shown in figures 2(f) and (g). In synergy, the optical performance assigned to NIR-SW could be reconfigurable between a high-clarity state and a low-clarity state by alternately loading the stress and NIR stimulus, as shown in figures 2(h) and (i) (supporting information, movie S2). As such, current wettability/light manipulator with shape-memory feature, remote control manner and energy-efficient merit would greatly boost its potential in water-proof envelope.

2.2. Shape-morphing thermodynamics over dual-mode NIR-SW

To impressively elucidate the shape-morphing thermodynamics over NIR-SW as a dual-functional actuator, a visual shape-memory process including shape fixing and shape reconfiguration was shown as figure 3(a). That is, when the CB/SMP is exposed to a natural temperature below T_g , the molecular motion of the polymer chains and polymer segments is frozen. Above T_g under the irradiation of NIR light, parts of the polymer chain are thermally activated to be locomotive with the help of photothermal effect arising from the embedded CB nanoparticles [42–45]. Therein, we in-situ press the SMP chains towards their entropically temporary state, and

then decrease their surface temperature below T_g to immobilize the polymer chains in their freezing state. The permanent erect state could be successfully reconfigurable by harnessing a NIR reheating operation in situ. Wherein, the targeted T_g assigned to CB/SMP could be verified at 90 °C depending on the dynamic mechanical analysis (DMA) method, as shown in figure 3(b).

In parts of figures 3(c) and (d), by using the thermal infrared imaging technique, we systematically study the relationship of surface temperature as a function of NIR loading duration for NIR-SWs with various CB-doped concentrations (C) and NIR-irradiating distance (d). For five NIR-SWs with C of 2, 5, 20, 30 and 50 mg·ml⁻¹, the time constant (τ) of rising from room temperature (~ 25 °C) to targeted T_g (~ 90 °C) was respectively quantified as 2.55, 2.33, 1.89, 1.67 and 1.33 min, where d was set as a constant ~ 18 cm (figure S2). When we installed $C = 50$ mg·ml⁻¹, NIR-SWs with different d values possessed τ as 0.55, 0.67, 0.78, 1.0 and 1.33 min, respectively. The results unfold that, the more dose of CB nanoparticles doped and the closer distance of NIR lamp located, the higher temperature of NIR-SW harvested. On above basis, we further investigated the shape-morphing dynamics over NIR-SW with variable pressure (1 N–5 N) and surface temperature (100 °C–130 °C) through a home-made CCD monitoring system (figures 3(e), (f) and S3; supporting information, movie S3). As the elevation of the surface temperature, the recovery rate of microwalls would increase from 1.5 to 1.9, 2.6 and then 5.0 degrees per second, where NIR-SW exhibits the same $\Delta\alpha \approx 45^\circ$ (figure 3(e)). In regard of loading force (F), the larger F was conducive for a larger bending extent α as well as a greater shape-morphing amplitude $\Delta\alpha$ (figure 3(f)). Significantly, cyclic pressing/photothermal maneuverer would not lead to the invalidation of microwalls, signifying current NIR-SW has an excellent fatigue resistance (figure 3(g)). Owing to its all-solid-state merit, NIR-SW presents an ultra-robust endurance over the continuously violent raindrop's impacting more than 10 000 cycles (supporting information, movie S4). In addition, current device was demonstrated to have a durable reliability even under long-term sunshine exposure which was well consistent with previous deployments (figure S7) [46, 47]. Otherwise, once the device's open channel was contaminated by dusts, we could readily clean it through ethanol rinsing owing to their good affinity.

2.3. Locomotion hydrodynamics over diverse droplets on NIR-SW

Optical window with tunable wettability is very favourable for expanding their potentials in drops condensation, anti-fouling, self-cleaning, anti/de-icing and so on [48–50]. Since current NIR-SW had manifested a switchable wettability between a slippery state and a sticky state, the steering hydrodynamics was studied by using a high-speed camera with high-frame-rate. As shown in figure 4(a), the upper time-lapse images displayed the water droplet (~ 10 μ L) vertically bouncing on a bent-mode NIR-SW, which exhibited an immense viscous

force and tightly pinned the surface drop. In sharp contrast, the lower 'pancake bouncing' phenomenon witnessed that the erect-mode NIR-SW had an ultra-robust water-proof capability. We manually sketched the drop's jumping trajectory on dual-mode NIR-SW, where we could detect the bending microwalls have a longer wetting ridge (L) and a lower jumping height (H) comparing to that of the erect microwalls (figures 4(b) and (c)). Above results further indicate that NIR-SW acts as not only an optical window but also a wettability manipulator.

Considering that the wetting property of NIR-SW should be highly dependent on the microwalls' topography, so we systematically study the effect of their interval on the WCA and WSA. As the interval gradually increased from 0.3 mm to 0.7 mm, the WCA for the drops (~ 10 μ l) on the erect microwalls and the bent microwalls were approximately measured as 165°, 161°, 156°, 151°, 147° and 132°, 134°, 132°, 133°, 134° (figure 4(d)) respectively. The larger the microwalls' interval is, the inferior the surface hydrophobicity. For five NIR-SWs with different intervals, their WSA for the droplets on erect-mode surface was approximately recorded as 7°, 10°, 12°, 16° and 20° (figure 4(e)), respectively. The larger the microwalls' interval was, the more arduous the surface droplets migrating. Comparatively, the drops tend to pin on these five bending surfaces. Significantly, current NIR-SW was widely adaptive for regulating the wettability of organic liquid species including milk, ethylene glycol (EG) and coffee, in addition to inorganic water drops (figures 4(f) and (g)). The switching hydrodynamics should be determined by the adhesion force at the interface of microwalls and drops (F_a), which was empirically defined as the surface tension of droplet (γ) multiply by the three-phase contact line (TCL) [51, 52]. Since the superhydrophobic erect microwalls had very limited TCL relative to that of the bent microwalls. F_a for the former (0.35 μ N) is far smaller than that of the later (0.89 μ N), which could be quantitatively uncovered via a home-made automatic tension dynamometer (figure 4(h)).

2.4. Study of dimming principle over dual-state NIR-SW

The microwalls' topography influenced not only the surface wettability of NIR-SW but also the interfacial optical performance. In this consideration, we could employ the UV-visible spectrum to investigate the optical transparency as a function of microwalls' interval assigned to dual-mode NIR-SW (figures 5(a), (b) and S4). As the increase of their interval, the optical transmittance at 550 nm (T_{550}) for the bent-mode and erect mode NIR-SW was respectively denoted as 0.05%, 0.1%, 0.4%, 6.2%, 17.0% and 24.0%, 38.3%, 44.8%, 54.4%, 60.7% (figure 5(c)). The larger the microwalls' interval was, the more superior the optical visibility. Seen from the reflectance spectrum as well as the absorption spectrum in figures 5(d) and (e), the enlarging of the microwalls' spacing interval would contribute to the reinforcement of interfacial reflectance (R) yet recede the light absorption intensity (A). Typically, for the NIR-SW featuring with the interval of 0.5 mm, the optical property including A , T and R assigned to

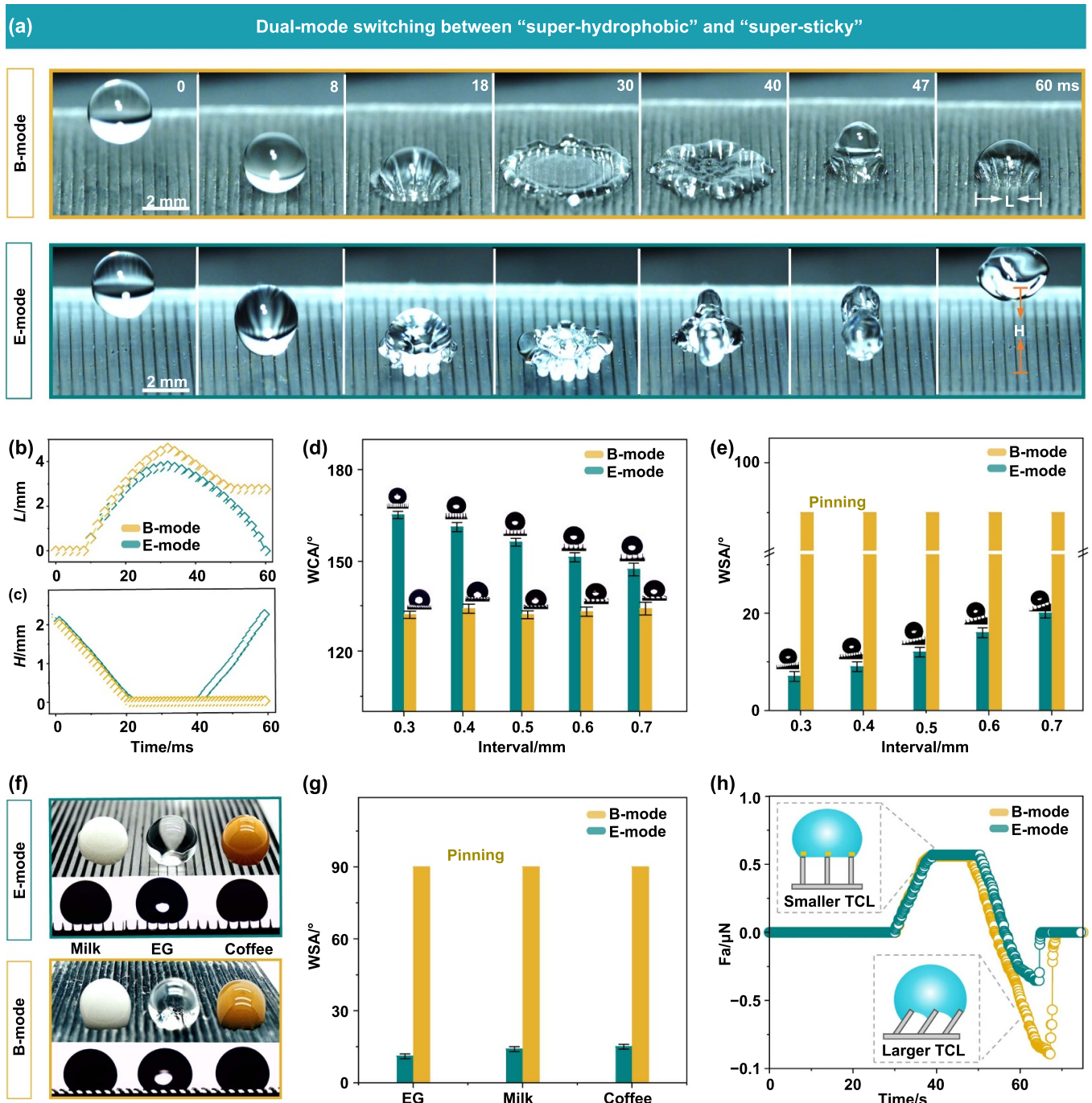


Figure 4. Switching hydrodynamics over diverse liquids on NIR-SW. (a) Time-lapse clips for monitoring the dynamics of a droplet (~10 ml) impacting on the bent-mode (upper row) and erect-mode (lower row) NIR-SW, where the drop’s released height was mounted at ~20 cm. The result witnesses that the open NIR-SW has a good super-repellence to droplets arising from the emerge of pancake bouncing, while the closed NIR-SW has intense stiction over the surface drops. The traced trajectory of the drops impacting on dual-mode NIR-SW including their (b) spreading length L and (c) bouncing height H . The change of (d) water contact angle and (e) water sliding angle with the increase of shutter’s interval. The larger the microwalls interval, the smaller the E-mode WCA but the elevated WSA. (f) Digital pictures for displaying the wetting performance of diverse organic liquids on dual-mode NIR-SW including milk, EG and coffee. The result unfolds that current NIR-SW is repellent to the inorganic as well as organic liquid species, thereby preventing the most sewages in reality. (g) The corresponding sliding angle SA for the diverse liquids on this dual-mode NIR-SW. (h) Comparison of the adhesion force F_a assigned to a bent-state NIR-SW and an erect-state one; the insets represent the physical model for illustrating the interfacial dynamics over the wettability-switching principle, signifying the TCL dominates the steering kinetics.

erect mode and bent mode were respectively recorded as 0.5%, 45%, 33% and 0.9%, 0.4%, 12% (figure 5(f)). Accordingly, current NIR-SW has a strong photothermal effect ascribing

to the embedded CB nanoparticles, which should be beneficial for anti/de-icing applications in a cold snowy climate [53–55]. We could actuate these shape-memory photothermal

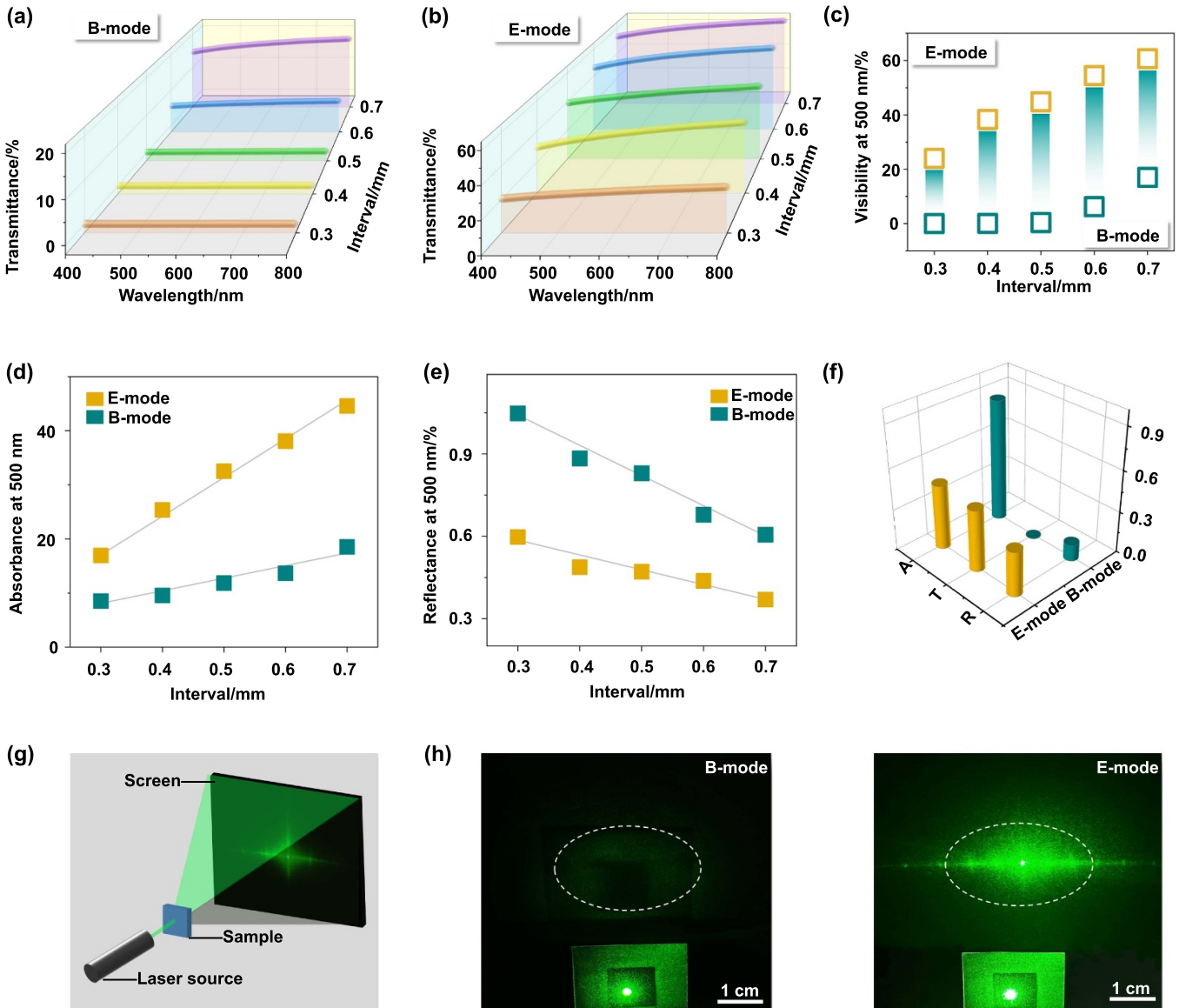


Figure 5. Optical regulating performance over dual-mode NIR-SW. The UV-Visible curves evolution for (a) B-mode and (b) E-mode NIR-SW with interval values increasing from 0.3 to 0.4, 0.5, 0.6 and then 0.7 mm. (c) Comparison of the optical transmittance at 550 nm for five dual-mode NIR-SW. The larger the microwalls interval, the larger the optical clarity. The sharp contrast of (d) absorption and (e) reflectance for dual-mode NIR-SW with a fixed interval of 0.6 mm. (f) 3D profile for comprehensively comparing the optical properties of current dual-state NIR-SW, implying the reflectance affects the clarity of E-mode NIR-SW and the absorption dominates the apperency of B-mode NIR-SW. (g) Schematic diagram for a home-built dimming apparatus including a laser source, NIR-SW shutter and a background filmset. (h) Digital clips for evidencing the NIR-SW serving as an optical shutter.

microwalls to evolve between an upstanding state and a curving state, thereby releasing and imprisoning the incident light according to the user’s requirement (figures 5(g) and (h)).

2.5. Thermal management, anti-icing, peep-proof screen and programmable optics display on a single versatile NIR-SW

As people anticipate that their roof or skylight could behave as an indoor thermo-regulating shutter for selectively cooling in the hot summer or warming in a cold winter depending on the imprison or leakage of solar energy input. As a proof

of paradigm, a home-built thermo-control system composed of solar simulator, various shelters, indoor CB-doped photo-thermal butterfly and a thermal infrared imaging camera was employed to examine and detect the temperature evolution of a greenhouse with the shelters of air, glass, erect-state and bent-state NIR-SW (figure 6(a)). The infrared camera automatically recorded the temperature-time curves of the indoor object, where the temperature plateaux over above four isolate shelters were respectively obtained as 44.9 °C, 39.4 °C, 36.3 °C and 29.0 °C (figures 6(b) and (c)). That is, comparing to the conventional glass window, current NIR-SW is more

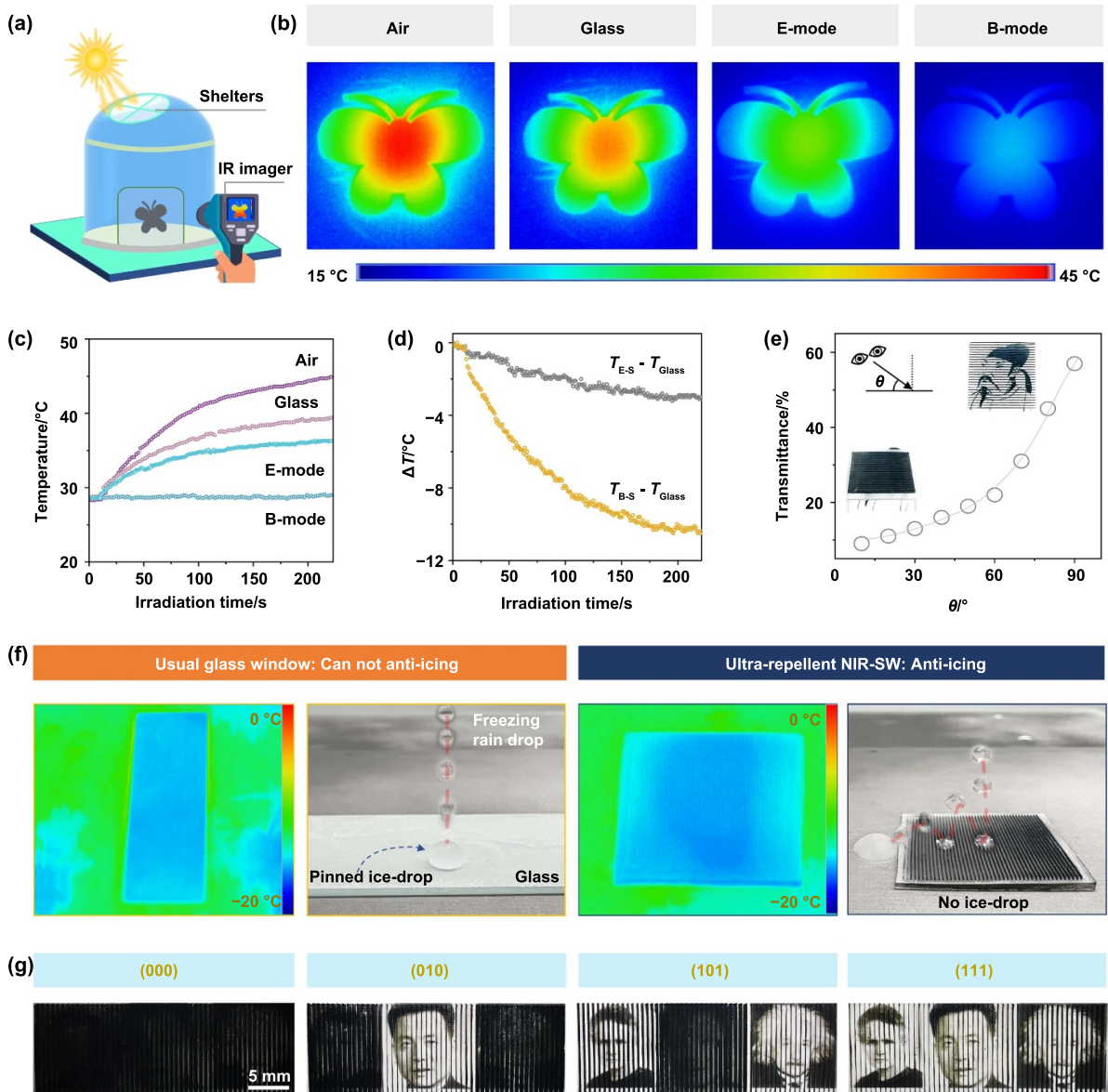


Figure 6. Proof-of-concept display upon all-in-one NIR-SW. (a) Schematic diagram for a home-made on-site temperature test system including solar simulator, hand-hold IR imager, an indoor photothermal object of CB-doped membrane, and the covered shelters. (b) Thermal infrared images at the saturation temperature and (c) real-time recorded temperature for four shelters of air, usual glass, E-mode and B-mode NIR-SW. (d) Comparison of temperature difference between the dual-mode NIR-SW and the usual glass. The result unfolds that current NIR-SW is more competent for the thermal management relative to the conventional glass window. (e) Time-lapse images for the droplets (10 ml-drop^{-1}) released on the frozen surface ($-20 \text{ }^\circ\text{C}$) of glass window (left) and NIR-SW (right). (f) Dependence of the clarity as a function of the visual angle, suggesting its potential in privacy screen. (g) Digital photos for on-demand encoding a single NIR-SW via a customized mask.

adaptive for steering the indoor thermal comfort by cooling (B-state: repulse sunlight) or warming (E-state: release sunlight) selection (figure 6(d)). More importantly, via timely restraining the ice nucleation on the surface, NIR-SW unfolded an excellent merit of anti-icing by virtue of effectively bouncing the freezing rain droplets off the surface (figure 6(e)). Additionally, current NIR-SW also exhibited a potential in visual optics (e.g. peep-proof screen) attributing to its angle-dependent feature (figures 6(f) and S5; supporting information, movie S5). Otherwise, this versatile NIR-SW could be

readily programmable from (000) to (111) through a well-designed shading mask, thereby encrypting/decrypting any desirable regions on demand (figure 6(g); supporting information, Movie S6). Above all-in-one functionalities should be attributed to the ideal design of light-responsive shape-memory micro-structures in addition to the feasible manipulating strategy. As comparison with the previous SWs, current light-triggered NIR-SW with superior comprehensive performance as well as unconventional steering manner conferred a new paradigm for energy-efficient SWs (figure S6).

3. Conclusion

In summary, we developed an ultradurable and energy-saving NIR-SW through the unity of laser-printing and soft lithography technology. Via harnessing the photothermal effect, the shape-memory microwalls impart NIR-SW with a dynamic glazing appearance under alternate NIR/stress stimulus. The underlying kinetics is the bent microwalls by stress display a longer TCL and a higher absorption accountable for a tremendous hysteresis (pinning at 90°) and an ultralow clarity $\sim 0.05\%$ at 550 nm. Once the NIR light was remotely loaded, the bent microwalls would recover to its erect state so as to harvest a high clarity $\sim 60\%$ and a smaller WSA $\sim 7^\circ$. In addition, we systematically study the influence of microwalls' topography on the wetting and optical performance of diverse NIR-SWs. More importantly, taking advantage of its all-solid-state feature, NIR-SW unfolds an unparalleled tolerance over the unceasing violent raindrop's impacting more than 10 000 cycles. Notably, relative to the previously-reported slippery SWs, current NIR-SW displays versatile functionalities over thermal management, anti-icing system, peep-proof screen and programmable optics. This work opens avenue for the domains of micro/nano-fabrications, antifouling optics, self-cleaning intelligent windows, energy-saving greenhouse, etc.

4. Experimental section

Materials. The CB particles ($\sim 99.99\%$ purity) with a mean size of 30 nm were purchased from Suzhou Shengernuo Technology Co., Ltd The SMP consisted of a matrix of bisphenol-type epoxy resin precursor together with a polyether-amine-230 curing agent was donated by Kunshan Julimei Electronic Materials Co., Ltd The PTFE film served as a template was purchased from Yangzhong Xingfuda Rubber & Plastic Co., Ltd The release agent was provided by Wuhan Jieguan Biotechnology Co., Ltd The NIR laser with wavelength, power, and spot area of 808 nm, 300 mW, and 3×2 mm, respectively, was purchased from Standing Laser, Shenzhen, China. Ethylene glycol (EG) was obtained from Sinopharm Chemical Reagent Co., Ltd

Laser-writing micro-grooved PTFE matrix: the PTFE membrane with the thickness of 0.5 mm was exposed to a focal Ti: Sapphire femtosecond laser scanning system (Legend Elite-1 K-HE, Coherent, USA). Wherein, the laser scanning manner was set as a line-by-line trajectory. Typically, the scanning parameters over the power density, scanning rate, scanning extent and scanning loop were fixed as 350 mW, $2 \text{ mm}\cdot\text{s}^{-1}$, 2 cm and 30 cycles, where the distances between two adjacent microgrooves were regulated as 0.3, 0.4, 0.5, 0.6 and 0.7 mm, respectively. The obtained micro-grooved matrix was harvested as a stamp for a subsequent replication procedure.

Preparation of CB/SMP hybrid: firstly, 10 g epoxy resin precursor could easily hybrid with 3 g curing agent under




a gentle stirring equipment for 5 min at room temperature, thereby harvesting a homogeneous SMP matrix. Thereafter, the as-prepared shape memory polymer matrix and CB nanoparticles were thoroughly blended with ratios of 2:0.1, 3:0.1, 5:0.1, 20:0.1, and 50:0.1 (wt%). Finally, the hybrid of CB/SMP could be successfully obtained through degassing in a vacuum chamber over 20 min to eliminate the tiny bubbles.

Characterization. The topography of laser-printed photothermal micro-walls was captured through a field-emission SEM (JSM-6700 F). 3D images for monitoring the surface morphology of NIR-SW were characterized via a laser scanning confocal microscope (OLS5100, Olympus). The dynamic clips of a water drop ($\sim 10 \mu\text{l}$) bouncing on the dual-state NIR-SW were recorded using a high-speed camera coupling with a long-distance microscope tube with a $2\times$ magnification objective (Photron-SA3&Mitutoyo). The high-speed videos were recorded by a rate of 6 400 fps and shutter speed of $1/200\ 000$ s. Critical slipping angles and contact angles of diverse droplets were measured utilizing the CA100C contact-angle system (Innuo) at 10% humidity and room temperature. Optical curves for various NIR-SW were recorded by UV/Visible spectrometer (Shimadzu Corporation 2501PC/2550, Japan). The optical spectrums for displaying the dependence of transmittance as a function of visual angle were harvested by a UV-VIS-NIR spectrophotometer (Agilent carry 5000). Solar irradiation source employed in the thermal management experiment was enabled via a solar simulator (CME-Sol 8150, China). Series temperature-time curves were donated from a thermal infrared camera (Fotric 348X, China). Digital images were captured by a mobile phone (iphone-8 plus, 7 mega-pixel).

Acknowledgment

This work was supported by the National Natural Science Foundation of China (No. 52005475, 62305321) and the Natural Science Foundation of Anhui Province (No. JZ2024AKZR0561, 2308085QE167) and Opening Project of the Key Laboratory of Bionic Engineering (Ministry of Education), Jilin University (K202204).

ORCID iDs

Chao Chen  <https://orcid.org/0000-0002-8061-0292>
 Chenchu Zhang  <https://orcid.org/0000-0002-3433-598X>
 Dong Wu  <https://orcid.org/0000-0003-0623-1515>

References

- [1] Hu S, Yan D, Guo S Y, Cui Y and Dong B 2017 A survey on energy consumption and energy usage behavior of households and residential building in urban China *Energy Build.* **148** 366–78
- [2] Kammen D M and Sunter D A 2016 City-integrated renewable energy for urban sustainability *Science* **352** 922–8

- [3] Ke Y J, Li Y B, Wu L C, Wang S C, Yang R G, Yin J, Tan G and Long Y 2022 On-demand solar and thermal radiation management based on switchable interwoven surfaces *ACS Energy Lett.* **7** 1758–63
- [4] Mufutau Opeyemi B 2021 Path to sustainable energy consumption: the possibility of substituting renewable energy for non-renewable energy *Energy* **228** 120519
- [5] Pablo-Romero M D P, Pozo-Barajas R and Yñiguez R 2017 Global changes in residential energy consumption *Energy Policy* **101** 342–52
- [6] Wang S C, Jiang T Y, Meng Y, Yang R G, Tan G and Long Y 2021 Scalable thermochromic smart windows with passive radiative cooling regulation *Science* **374** 1501–4
- [7] Casini M 2018 Active dynamic windows for buildings: a review *Renew. Energy* **119** 923–34
- [8] Tang K C et al 2021 Temperature-adaptive radiative coating for all-season household thermal regulation *Science* **374** 1504–9
- [9] Llordés A, Garcia G, Gazquez J and Milliron D J 2013 Tunable near-infrared and visible-light transmittance in nanocrystal-in-glass composites *Nature* **500** 323–6
- [10] Gu C, Jia A B, Zhang Y M and Zhang S X A 2022 Emerging electrochromic materials and devices for future displays *Chem. Rev.* **122** 14679–721
- [11] Ke Y J, Chen J W, Lin G J, Wang S C, Zhou Y, Yin J, Lee P S and Long Y 2019 Smart windows: electro-, thermo-, mechano-, photochromics, and beyond *Adv. Energy Mater.* **9** 1902066
- [12] Islam S M, Hernandez T S, McGehee M D and Barile C J 2019 Hybrid dynamic windows using reversible metal electrodeposition and ion insertion *Nat. Energy* **4** 223–9
- [13] Guo J, Wu S S, Wang Y L, Huang J H, Xie H and Zhou S B 2022 A salt-triggered multifunctional smart window derived from a dynamic polyampholyte hydrogel *Mater. Horiz.* **9** 3039–47
- [14] Chen S, Jiang G Y, Zhou J H, Wang G, Zhu Y, Cheng W K, Xu G W, Zhao D W and Yu H P 2023 Robust solvatochromic gels for self-defensive smart windows *Adv. Funct. Mater.* **33** 2214382
- [15] Son J, Kim J A, Joo B S, Lee W Y, Kang J, Han I K, Jang H S, Ko H and Kang G M 2023 A mechanoresponsive smart window based on multifunctional luminescent solar concentrator *Sol. RRL* **7** 2300445
- [16] Wang S C, Dong Y T, Li Y B, Ryu K, Dong Z L, Chen J, Dai Z D, Ke Y J, Yin J and Long Y 2023 A solar/radiative cooling dual-regulation smart window based on shape-morphing kirigami structures *Mater. Horiz.* **10** 4243–50
- [17] Shrestha M, Lau G K, Asundi A and Lu Z B 2021 Dielectric elastomer actuator-based multifunctional smart window for transparency tuning and noise absorption *Actuators* **10** 16
- [18] Shrestha M, Lau G K, Bastola A K, Lu Z, Asundi A and Teo E H T 2022 Emerging tunable window technologies for active transparency tuning *Appl. Phys. Rev.* **9** 031304
- [19] Shrestha M, Lau G K, Asundi A and Lu Z B 2020 Multifunctional smart window based on dielectric elastomer actuator *Proceedings* **64** 32
- [20] Shrestha M, Asundi A and Lau G K 2018 Smart window based on electric unfolding of microwrinkled TiO₂ nanometric films *ACS Photonics* **5** 3255–62
- [21] Li J N, Lu X G, Zhang Y, Ke X Q, Wen X X, Cheng F, Wei C P, Li Y L, Yao K K and Yang S 2021 Highly sensitive mechanoresponsive smart windows driven by shear strain *Adv. Funct. Mater.* **31** 2102350
- [22] Li Y C, Wang M M, Zhang C, Wang C C, Xu W H, Gao S W, Zhou Y S, Wang C T and Wang Z K 2022 A fully self-powered cholesteric smart window actuated by droplet-based electricity generator *Adv. Opt. Mater.* **10** 2102274
- [23] Chen G Q et al 2023 Printable thermochromic hydrogel-based smart window for all-weather building temperature regulation in diverse climates *Adv. Mater.* **35** 2211716
- [24] Alqurashi T and Butt H 2019 Highly flexible, stretchable, and tunable optical diffusers with mechanically switchable wettability surfaces *ACS Cent. Sci.* **5** 1002–9
- [25] Lee S H, Kang B S and Kwak M K 2022 Magneto-responsive actuating surfaces with controlled wettability and optical transmittance *ACS Appl. Mater. Interfaces* **14** 14721–8
- [26] Nakamura C, Manabe K, Tenjimbayashi M, Tokura Y, Kyung K H and Shiratori S 2018 Heat-shielding and self-cleaning smart windows: near-infrared reflective photonic crystals with self-healing omniphobicity via layer-by-layer self-assembly *ACS Appl. Mater. Interfaces* **10** 22731–8
- [27] Yao X, Hu Y H, Grinthal A, Wong T S, Mahadevan L and Aizenberg J 2013 Adaptive fluid-infused porous films with tunable transparency and wettability *Nat. Mater.* **12** 529–34
- [28] Yao X, Ju J, Yang S, Wang J J and Jiang L 2014 Temperature-driven switching of water adhesion on organogel surface *Adv. Mater.* **26** 1895–900
- [29] Manabe K, Matsubayashi T, Tenjimbayashi M, Moriya T, Tsuge Y, Kyung K H and Shiratori S 2016 Controllable broadband optical transparency and wettability switching of temperature-activated solid/liquid-infused nanofibrous membranes *ACS Nano* **10** 9387–96
- [30] Owuor P S et al 2018 High stiffness polymer composite with tunable transparency *Mater. Today* **21** 475–82
- [31] Park J Y, Song H, Kim T, Suk J W, Kang T J, Jung D and Kim Y H 2016 PDMS-paraffin/graphene laminated films with electrothermally switchable haze *Carbon* **96** 805–11
- [32] Li M J, Yang T Z, Yang Q, Wang S K, Fang Z, Cheng Y, Hou X and Chen F 2023 Slippery quartz surfaces for anti-fouling optical windows *Droplet* **2** e41
- [33] Yin K, Wu J R, Deng Q W, Wu Z P, Wu T N, Luo Z, Jiang J and Duan J A 2022 Tailoring micro/nanostructured porous polytetrafluoroethylene surfaces for dual-reversible transition of wettability and transmittance *Chem. Eng. J.* **434** 134756
- [34] Chen C, Yao H, Guo S J, Lao Z X, Xu Y D, Li S Y and Wu S Z 2023 Ultra-robust joule-heated superhydrophobic smart window: dually-switching droplets adhesion and transparency via in situ electric-actuated reconfigurable shape-memory shutters *Adv. Funct. Mater.* **33** 2210495
- [35] Chen C, Chen Y, Yao H, Song Q R, Jia C and Zhang Y C 2022 A dual-mode laser-textured ice-phobic slippery surface: low-voltage-powered switching transmissivity and wettability for thermal management *Nanoscale* **14** 4474–83
- [36] Chen C et al 2019 In situ reversible control between sliding and pinning for diverse liquids under ultra-low voltage *ACS Nano* **13** 5742–52
- [37] Chen C, Huang Z C, Zhu S W, Liu B R, Li J W, Hu Y L, Wu D and Chu J R 2021 In situ electric-induced switchable transparency and wettability on laser-ablated bioinspired paraffin-impregnated slippery surfaces *Adv. Sci.* **8** 2100701
- [38] Yao H and Chen C 2023 Ultrarobust, highly sensitive and swinging-independent droplets-spatial manipulator enabled via laser-printed magnetically actuated shape-morphing microshutters *Adv. Intell. Syst.* **5** 2300375
- [39] Yang P Y, Yin K, Song X H, Wang L X, Deng Q W, Pei J Q, He Y C and Arnusch C J 2024 Airflow triggered water film self-sculpturing on femtosecond laser-induced heterogeneously wetted micro/nanostructured surfaces *Nano Lett.* **24** 3133–41
- [40] Huang Q Q, Yin K, Wang L X, Deng Q W and Arnusch C J 2023 Femtosecond laser-scribed superhydrophilic/superhydrophobic self-splitting patterns for one droplet multi-detection *Nanoscale* **15** 11247–54

- [41] Wu T N, Yin K, Pei J Q, He Y C, Duan J A and Arnusch C J 2024 Femtosecond laser-textured superhydrophilic coral-like structures spread AgNWs enable strong thermal camouflage and anti-counterfeiting *Appl. Phys. Lett.* **124** 161602
- [42] Bai X, Gou X D, Zhang J L, Liang J, Yang L J, Wang S P, Hou X and Chen F 2023 A review of smart superwetting surfaces based on shape-memory micro/nanostructures *Small* **19** 2206463
- [43] Omar M, Sun B H and Kang S H 2021 Good reactions for low-power shape-memory microactuators *Sci. Robot.* **6** eabh1560
- [44] Park J K et al 2019 Remotely triggered assembly of 3D mesostructures through shape-memory effects *Adv. Mater.* **31** 1905715
- [45] Ze Q, Kuang X, Wu S, Wong J, Montgomery S M, Zhang R D, Kovitz J M, Yang F Y, Qi H J and Zhao R K 2020 Magnetic shape memory polymers with integrated multifunctional shape manipulation *Adv. Mater.* **32** 1906657
- [46] Xia Y, He Y, Zhang F, Liu Y and Leng J 2021 A review of shape memory polymers and composites: mechanisms, materials, and applications *Adv. Mater.* **33** 2000713
- [47] Tan Q, Li F F, Liu L W, Liu Y J, Yan X Q and Leng J S 2019 Study of low earth orbit ultraviolet radiation and vacuum thermal cycling environment effects on epoxy-based shape memory polymer *J. Intell. Mater. Syst. Struct.* **30** 2688–96
- [48] Epstein A K, Wong T S, Belisle R A, Boggs E M and Aizenberg J 2012 Liquid-infused structured surfaces with exceptional anti-biofouling performance *Proc. Natl Acad. Sci. USA* **109** 13182–7
- [49] Kreder M J, Alvarenga J, Kim P and Aizenberg J 2016 Design of anti-icing surfaces: smooth, textured or slippery? *Nat. Rev. Mater.* **1** 15003
- [50] Park K C, Kim P, Grinthal A, He N, Fox D, Weaver J C and Aizenberg J 2016 Condensation on slippery asymmetric bumps *Nature* **531** 78–82
- [51] Wu S Z, Wang Y, Chen C, Peng Y B, Li L F, Zhang Y Y, Wang D W, Li Z C, Li C Z and Zhang C C 2021 Carbon black-based NIR-responsive superhydrophobic shape memory microplate array with switchable adhesion for droplets and bubbles manipulation *Appl. Phys. Lett.* **119** 181601
- [52] Li C Z et al 2022 Laser-induced morphology-switchable slanted shape memory microcones for maneuvering liquid droplets and dry adhesion *Appl. Phys. Lett.* **120** 061603
- [53] He H, Huang W and Guo Z G 2023 Superhydrophobic and photothermal SiC/TiN durable composite coatings for passive anti-icing/active de-icing and de-frosting *Mater. Today Phys.* **30** 100927
- [54] Peng C, Yang D J, You Z P, Ruan D, Guan P W, Ye Z L, Ning Y F, Zhao N and Yang F Y 2024 A photothermal and superhydrophobic emulsified asphalt coating modified by CNTs and PTFE for anti-icing and de-icing applications *Constr. Build. Mater.* **416** 135148
- [55] Zhang L, Gao C L, Zhong L S, Zhu L M, Chen H, Hou Y P and Zheng Y M 2022 Robust photothermal superhydrophobic coatings with dual-size micro/nano structure enhance anti-/de-icing and chemical resistance properties *Chem. Eng. J.* **446** 137461